# Supplementary Information

# Role and Dynamics of Transition Metal Carbides in Methane Coupling

Seraphine B.X.Y. Zhang,[1] Quentin Pessemesse,[2] Lukas Lätsch,[1] Konstantin M. Engel,[1] Wendelin J. Stark,[1] Alexander van Bavel,[3] Andrew D. Horton,[3] Pierre-Adrien Payard,[2,*] Christophe Copéret[1,*]

[1]Department of Chemistry and Applied Biosciences, ETH Zurich, Vladimir-Prelog-Weg 2, 8093 Zurich, Switzerland

[2]Université Claude Bernard Lyon I, CNRS, INSA, CPE, UMR 5246, ICBMS, Rue Victor Grignard, F-69622 Villeurbanne Cedex, France

[3]Shell Global Solutions International B.V., Grasweg 31, 1031 HW Amsterdam, The Netherlands

# Contents

# 1 Overview of relevant literature for methane coupling under non-oxidative conditions

**Table S1:** Overview of relevant literature for methane coupling under non-oxidative conditions.

| year | reaction | cat. ([g]) | feed gas ([mL/min]) | T [K] | $CH_4$ conv. [%] | $C_2^+$ sel. [%] | ref. |
|---|---|---|---|---|---|---|---|
| 1993 | MDA | Mo/ZSM-5 (0.2) | $CH_4$ (30) | 973 | 7 | 100 ($C_6H_6$) | [1] |
| 2003 | MDA | Mo/ZSM-5 (0.2) | $CH_4$:$N_2$ 9:1 (5) | 1003 | 17 | 60 ($C_6H_6$) | [2] |
| 2008 | NOCM | Ta-H@$SiO_2$ (0.3) | $CH_4$ (3), 50 bar | 648 | 0.1 | 98 ($C_2H_4$) | [3] |
| 2010 | NOCM | W-H@$\gamma$-$Al_2O_3$ (0.5) | $CH_4$ (3), 50 bar | 623 | 0.2 | 99 | [4] |
| 2014 | NOCM | Fe©$SiO_2$ (0.75) | $CH_4$:$N_2$ 9:1 (10-30) | 1363 | 48 | 99 | [5] |
| 2016 | NOCM | Fe©$SiO_2$ (0.38) | $CH_4$:Ar 9:1(20) | 1323 | 30 | 99 | [6] |
| 2018 | NOCM | Pt©$CeO_2$ (0.2) | 1% $CH_4$ in He (20) | 1248 | 14 | 75 | [7] |
| 2018 | NOCM | PtBi alloy (0.5) | $CH_4$:$N_2$ 1:9(100) | 973 | 6 | 85 | [8] |
| 2019 | NOCM | Fe/$SiO_2$ (0.38) | $CH_4$:$N_2$ 9:1(20) | 1273 | 11 | 90 | [9] |
| 2020 | NOCM | Fe©$SiO_2$ (0.1) | $CH_4$:Ar 7.5:92.5 (200) | 1273 | 3 | 20 | [10] |

[a] The reactions were performed at a pressure of 1 bar unless otherwise noted.

# Materials and Methods

## 2 Synthesis

### 2.1 WC

$WO_3$ powder was synthesized by oxidative flame spray pyrolysis using a 7.9 wt% solution of $WCl_6$ (Acros Organics) in a 1:6 mixture of THF (LiChrosolv, Merck) and benzyl alcohol (for analysis, Sigma-Aldrich) as precursor. 5 mL/min of the latter were dispersed at a 0.4 mm nozzle with an oxygen flow of 5 NL/min into a support flame of $CH_4/O_2$ (2.4:1.2 NL/min). The resulting nanoparticles were collected on a GF/A-6 glass fiber filter and carburized by heating under a stream of $H_2$:$CH_4$ (80/20, v/v, 40 mL/min). The heating program was 1h to 300°C and then with 120°C/h to 1000°C, where the material was kept for one hour and then cooled down to RT yielding black tungsten carbide powder (hexagonal). The particle diameter was determined to be between 200-800 nm and the BET surface area is 3 $m^2/g$.

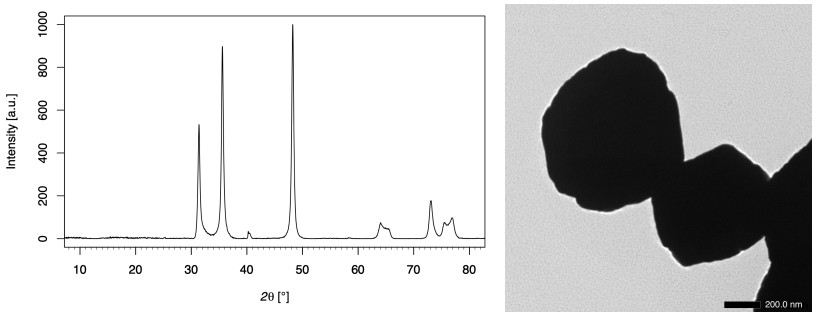


**(a)** **(b)**

**Figure S1:** (a) pXRD for WC (PDF 00-073-0471), (b) TEM of WC.

### 2.2 $Mo_2C$ nanorods

$Mo_2C$ nanorods were synthesized as previously reported.[11] 2.5 g ammonium heptamolybdate tetrahydrate ($(NH_4)_6Mo_7O_{24} \cdot 4\,H_2O$) was dissolved in 40 mL water containing 3.8 g p-methylaniline. Then, 1.0 M hydrochloric acid was added to adjust the pH value to 4.0. After reaction at 50 °C for 4 h in an oil bath, the precipitate was filtered, washed with water and ethanol, and then dried at 50 °C *in vacuo*. The above precursor was transferred into a tube furnace, and then heated at 1000 °C for 5 h under argon flow (30 mL/min). Finally, the $Mo_2C$ nanorods were harvested. The surface area was determined to be 21 $m^2/g$.

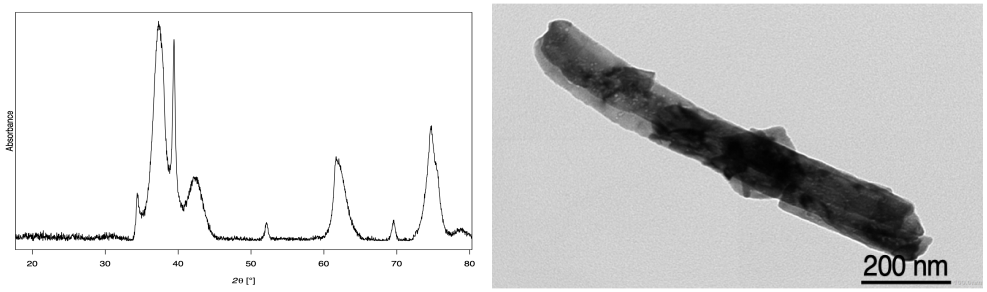


**(a)** **(b)**

**Figure S2:** (a) pXRD for $Mo_2C$ nanorods: $\beta$-$Mo_2C$ crystal structure. PDF:[00-035-0787], orthorhombic. (b) TEM picture of $Mo_2C$ nanorods.

# 3 Characterization

## 3.1 pXRD

X-Ray diffraction of the samples was performed with a STOE STADI P powder diffractometer, operating in transmission mode. A germanium monochromator, Cu K$\alpha$1 irradiation and Dectris Mythen silicon strip detector were used. $\beta$-Mo2C (PDF # 00-035-0787) and WC (PDF # 00-073-0471) structures were confirmed.

## 3.2 TEM

Images were recorded using a JEOL JEM- 2200FS microscope operated at 200 kV.

## 3.3 XPS

XPS analysis was performed at ETH Zurich using the SIGMA II instrument equipped with an Al/Mg twin source. The vacuum in the chamber was around 2x10$^8$ mbar during measurements. The analyses were carried out with a Mg-K$\alpha$ source (energy = 1253.6 eV) in LAXPS mode with a pass energy of 16 eV. The curvefitting was performed with CasaXPS using Shirley as background and a lineshape of GL(30).

### 3.3.1 $Mo_2C$ XPS

The Mo 3d 5/2 peak was fitted with two components found at 228.6 eV for the $Mo_2C$ ($Mo^{2+}$) component of $Mo_2C$ and 229.4 eV for the MoC ($Mo^{4+}$) component for the pristine as well as for the spent $Mo_2C$ with the major component being $Mo^{2+}$. This is in agreement with previous reports of $Mo_2C$ XPS reports.[12] The carbon component is split into three components: carbidic C with a binding energy of 283.6 eV, advantitious ($sp^2$) C at 284.8 eV and $sp^3$ C deposit at 285.3 eV. The fraction of C deposit increases for the spent $Mo_2C$.[13,14]

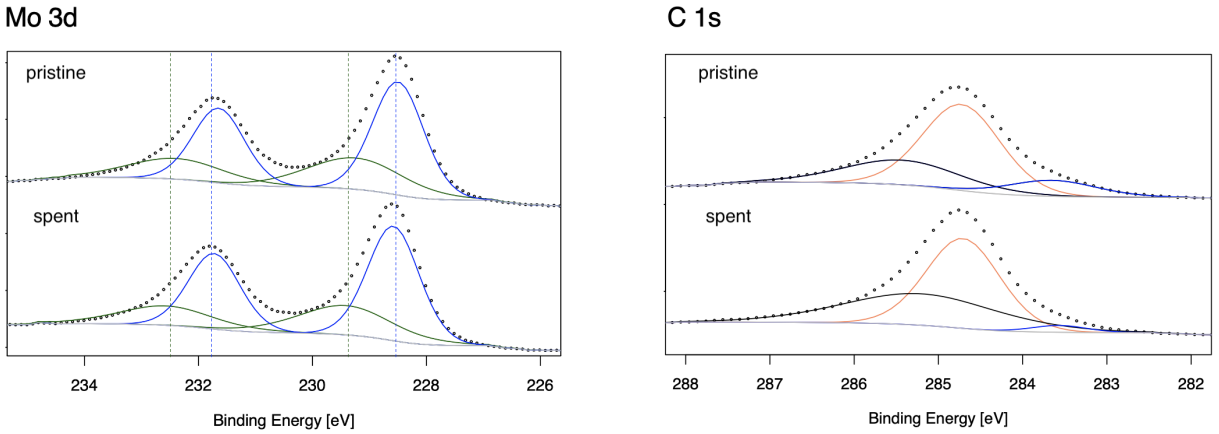


**Figure S3:** XPS Spectra for Mo 3d and C 1s components of $Mo_2C$.

### 3.3.2 WC XPS

The XPS spectra collected at the W 4f core level are shown in Figure S4. The spectra can be fitted on the basis of two multiplets that correspond to the W 4f 7/2 and W 4f 5/2 components which have a spin-orbit splitting of 2.2 eV. The WC ($W^{4+}$) peaks were identified at 32.5 and 32.7 eV for the pristine and the spent catalyst respectively. Pristine WC which was exposed to air shows a mixture of WC at 32.5 eV and $WO_3$ ($W^{6+}$) at a higher binding energy of 36.6 eV. In the spent WC, while no $WO_3$ was found, reduction to metallic W(0) with the 4f 7/2 component at 32.1 eV was observed. For W(0) metal a characteristic loss feature is reported, it can be observed here as a broad peak at 38 eV. Overall, XPS measurements show a change in composition for the surface from a mixture of $WO_3$ and WC in the pristine catalyst to WC and W(0) in the spent catalyst.

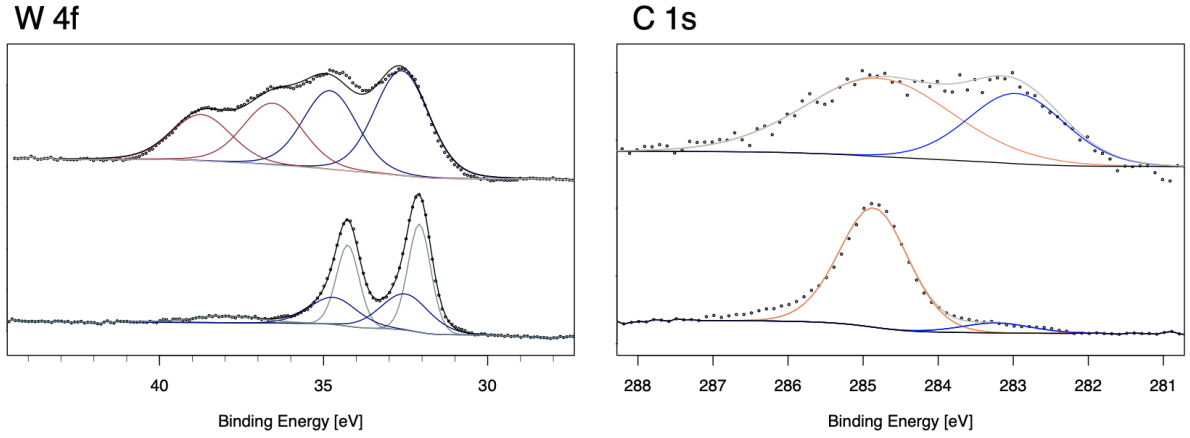


**Figure S4:** XPS Spectra for W 4f and C 1s components of WC.

## 3.4 $^{13}$C solid state MAS NMR

$^{13}$C solid state MAS NMR measurements were carried out using a Bruker 400 MHz NMR spectrometer operating at a frequency of 400 MHz. A 4.0 mm MAS NMR zirconia rotor was used with a spinning speed of 10 kHz. A spin echo sequence with a 5 $\mu$s $\pi/2$ pulse and a relaxation delay of 7s was applied. The spectra were recorded at room temperature and referenced with adamantane (38.4 ppm).

## 3.5 GCMS

The GCMS was calibrated with a gas mixture containing 0.5% acetylene, 5% ethane, 10% ethylene, 10% Helium, 15% hydrogen, 39.5% Ar and 20% methane. The following fragmentation patterns for $C_2$ products were obtained from the calibration and further on used for fitting the experimental pattern by adding m/z+1 for monolabelled $C_2$ species and by adding m/z+2 for dilabelled $C_2$ species.

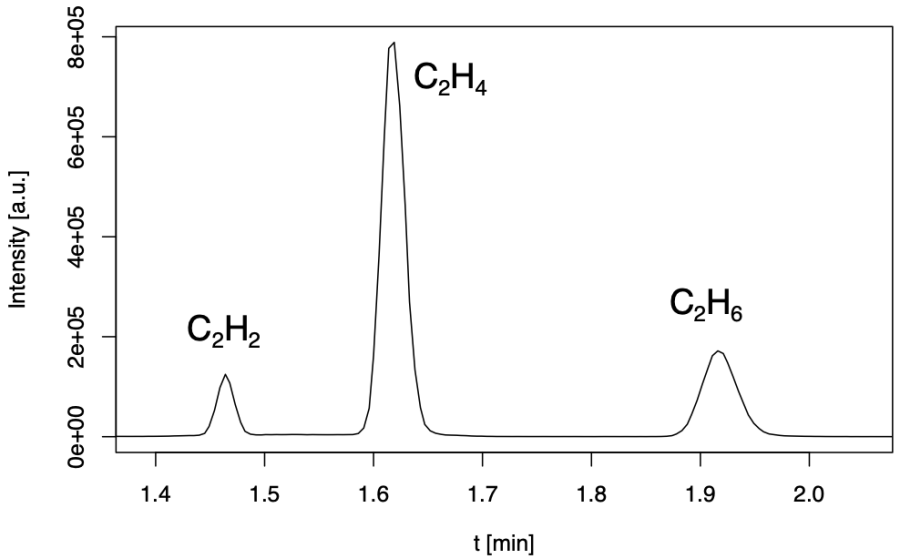


**Figure S5:** This GC trace shows the signals of acetylene (1.46 min), ethylene (1.62 min) and ethane (1.91 min) of the calibration.

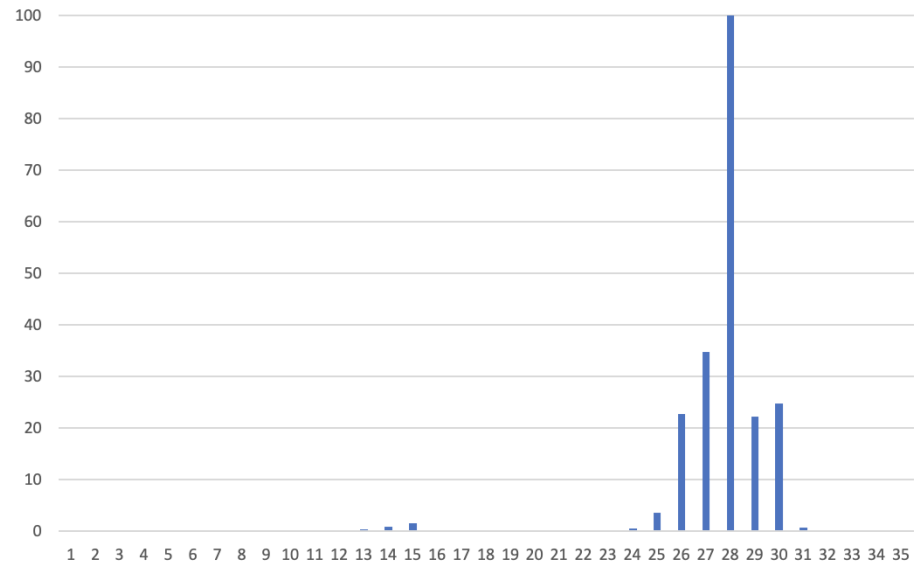


**(a)** Fragmentation pattern for ethane

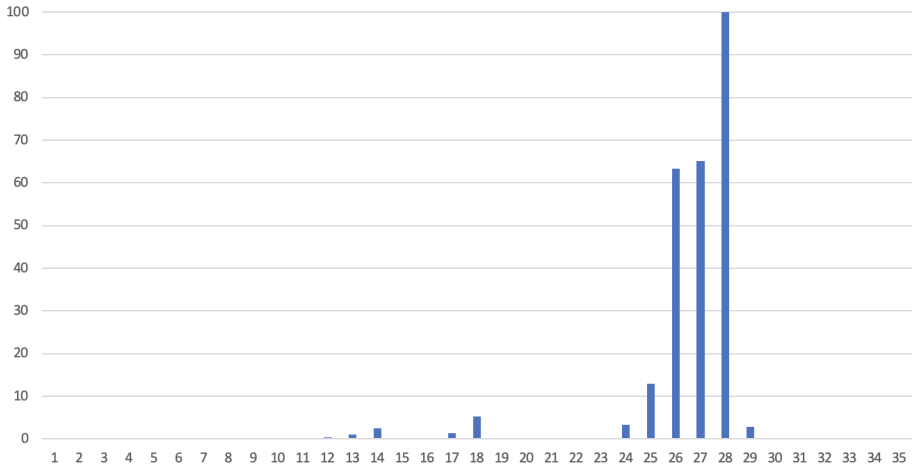


**(b)** Fragmentation pattern for ethylene

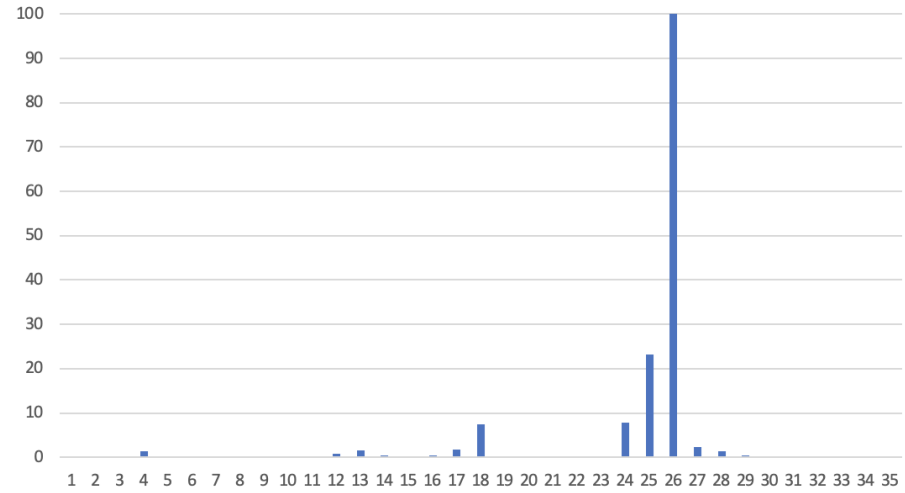


**(c)** Fragmentation pattern for acetylene

**Figure S 6:** Fragmentation patterns of $C_2$ species of calibration gas mixture. y axis: relative intensity [%], x axis: m/z.

### 3.5.1 GCMS Test

**Table S2:** Distribution of isotope-labelled $C_2$ products over contact time at 1100°C for $Mo_2C$ and WC.

| $Mo_2C$ | t [h] | $^{12}C$-$^{12}C$[%] | $^{12}C$-$^{13}C$[%] | $^{13}C$-$^{13}C$[%] | error[%] |
|---|---|---|---|---|---|
| $C_2H_6$ | 3 | 93 | 6 | 1 | 1 |
| | 6 | 95 | 2 | 3 | 2 |
| | 9 | 89 | 9 | 2 | 1 |
| | 12 | 89 | 7 | 4 | 2 |
| $C_2H_4$ | 3 | 95 | 4 | 1 | 1 |
| | 6 | 96 | 4 | 0 | 2 |
| | 9 | 94 | 6 | 1 | 2 |
| | 12 | 94 | 4 | 2 | 1 |
| WC | t [h] | $^{12}C$-$^{12}C$[%] | $^{12}C$-$^{13}C$[%] | $^{13}C$-$^{13}C$[%] | error[%] |
| $C_2H_4$ | 3 | 1 | 2 | 97 | 2 |
| | 6 | 1 | 1 | 98 | 1 |
| | 9 | 3 | 9 | 88 | 2 |
| | 12 | 9 | 14 | 77 | 1 |
| $C_2H_2$ | 3 | 2 | 2 | 96 | 1 |
| | 6 | 3 | 6 | 91 | 2 |
| | 9 | 5 | 14 | 81 | 1 |
| | 12 | 2 | 39 | 59 | 3 |

[a] The experiment to determine species distribution was performed in duplicates to ensure reproducibilty.

### 3.5.2 Fragmentation Pattern Fits

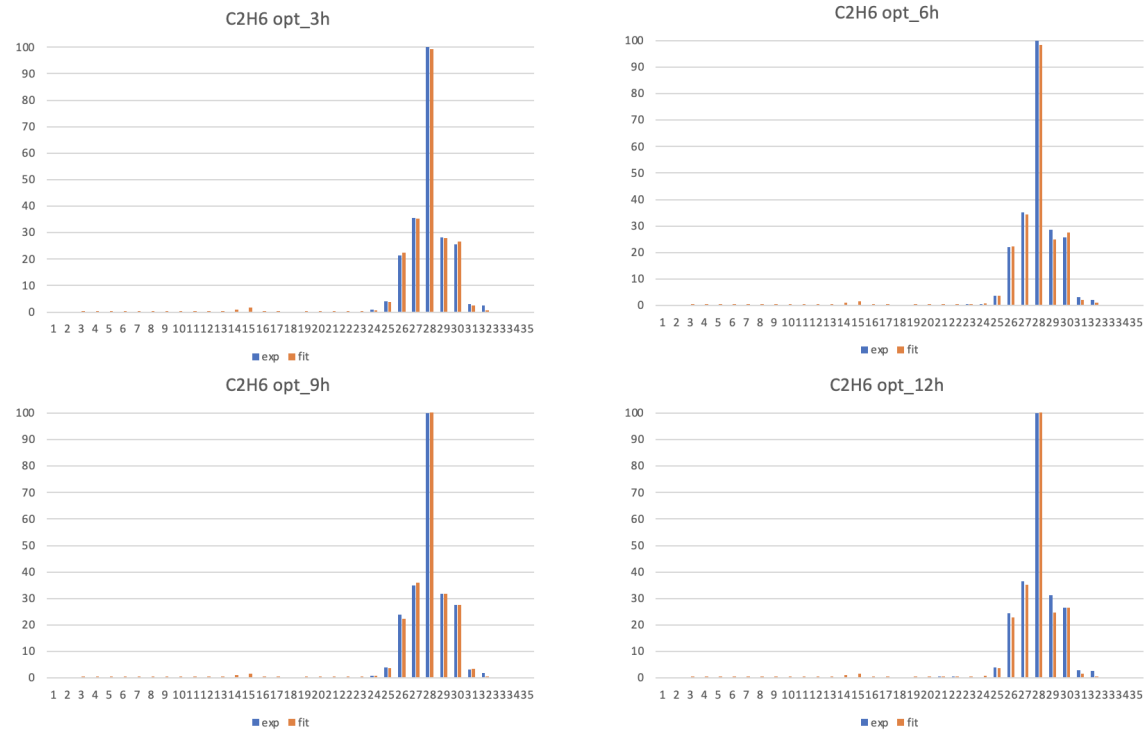


**(a)** Fragmentation patterns were fitted for $C_2H_6$ for the test with $Mo_2C$ and $^{13}CH_4$.

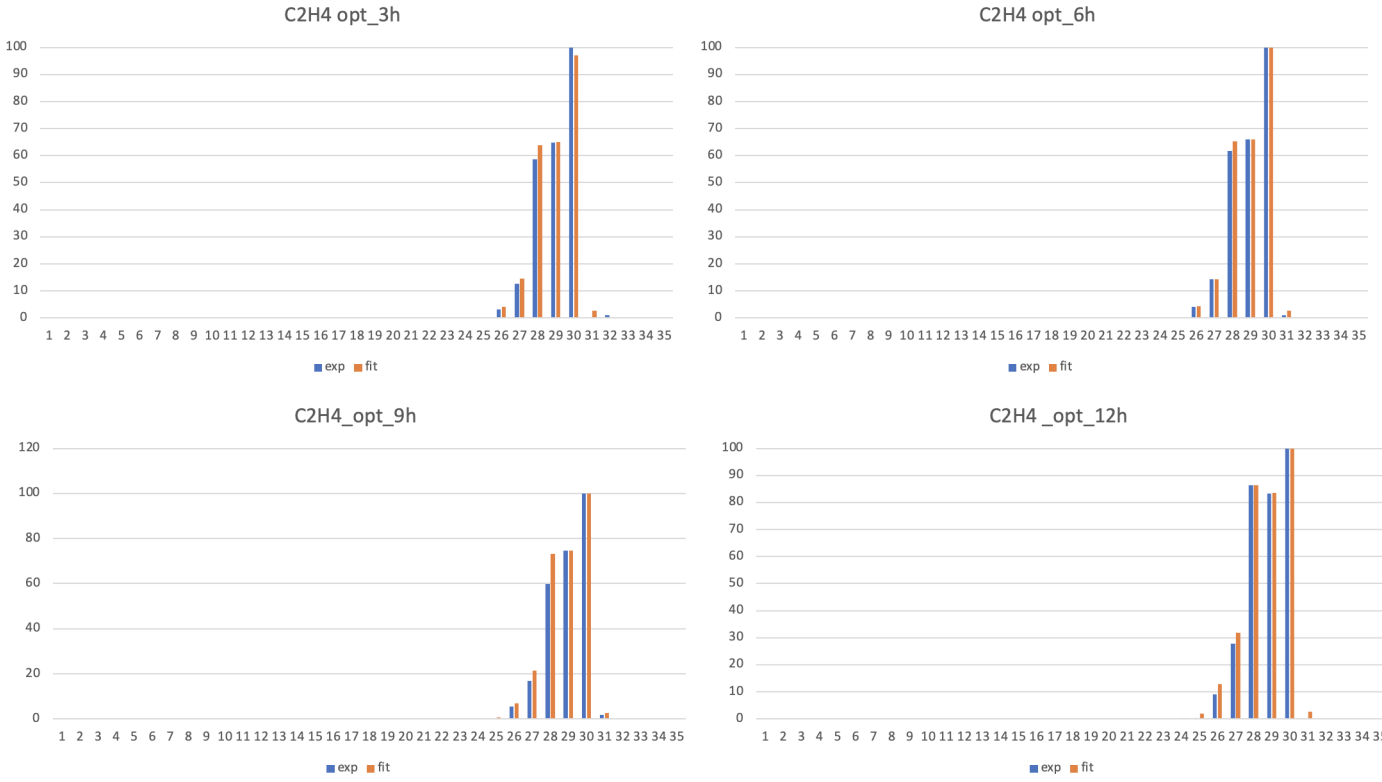


**(b)** Fragmentation patterns were fitted for $C_2H_4$ for the test with WC and $^{13}CH_4$.

**Figure S7**

# 4 Definitions for Methane Conversion, Product Selectivity and Yield

Methane conversion, products selectivity and yield are defined as previously reported.[8,15]

## $CH_4$ Conversion

Argon was used as an internal standard. The total gas flow rate at the outlet of the reactor ($\Phi_{outlet}$) was calibrated with equation (1) since the mass flow rate of non-reactive Ar as internal standard should be constant throughout the reaction.

$$\Phi_{tot}^{in} \cdot x_{Ar}^{in} = \Phi_{tot}^{out} \cdot x_{Ar}^{out} \tag{1}$$

$$\mathrm{CH_4\ conversion} = \frac{\Phi^{in} \cdot x_{CH_4}^{in} - \Phi^{out} \cdot x_{CH_4}^{out}}{\Phi^{in} \cdot x_{CH_4}^{in}} = 1 - \frac{x_{CH_4}^{out} \cdot x_{Ar}^{in}}{x_{CH_4}^{in} \cdot x_{Ar}^{out}} \tag{2}$$

## Product Selectivity

The selectivity was calculated as follows. It is accounted for the number of C with $N_C$ as the number of carbon atoms of the product.

$$S_P = \frac{x_{Ar}^{in} \cdot x_P^{out} \cdot N_C}{x_{Ar}^{out} \cdot x_{CH_4}^{in} - x_{Ar}^{in} \cdot x_{CH_4}^{out}} \tag{3}$$

$$S_{coke} = 1 - \Sigma S_P \tag{4}$$

## Product Yield

$$Y_P = CH_4\ \mathrm{conversion} \cdot S_P \tag{5}$$

# 5 Catalytic Testing

The catalytic performance tests were conducted in a fixed-bed quartz reactor with an inner diameter of 9 mm and a quartz frit. The temperature program was 900°C-1000°C-1100°C, each temperature was kept for 60 min. The heating rate was 100°C/min. The standard operating conditions were 0.1 g of catalyst, 10 v% of $CH_4$ in Argon and a GHSV of 24'000 $mL*g_{cat}^{-1}*h^{-1}$. Unless otherwise stated, all data sets are averages of 1 hr time on stream (TOS) at a given temperature.

## 5.1 Catalytic Test Setup

The catalytic test setup comprises an IR furnace which can work at upto 1300 °C under continuous operation. The gas feed can be chosen as any desired mixture of $CH_4$, $H_2$ and Ar. Analysis is performed with an Agilent 490 $\mu$-GC equipped with 2 columns and a TCD, the MS 5Å column (20 m) is used to separate permanent gases while the PPU column (10 m) allows the quantification of light hydrocarbons. The setup was used to analyse the methane coupling performance for WC and $Mo_2C$.

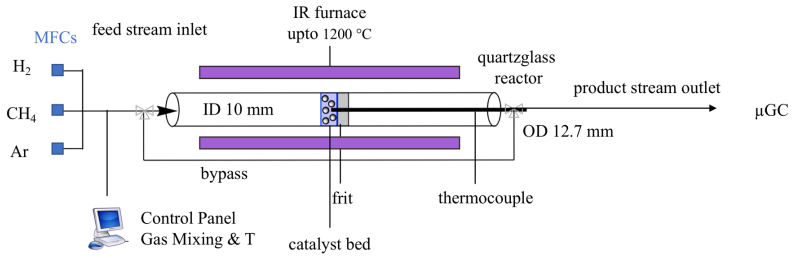


**(a)** Scheme of catalytic test setup with IR furnace and flow board with access to $CH_4$, $H_2$ and Ar.

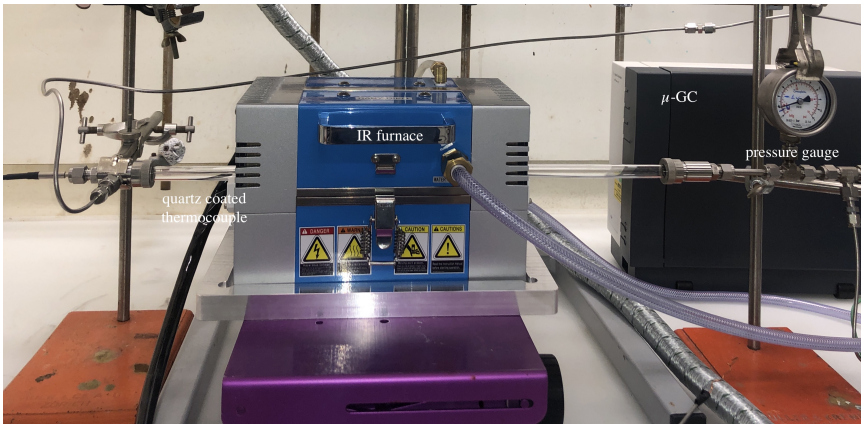


**(b)** Picture of catalytic test setup with IR furnace (with water cooling), quartz glass tube (ID 9 mm), $\mu$-GC Agilent 490 and quartz coated thermocouple.

**Figure S8:** Catalytic Test Setup

### 5.1.1 Blank Test

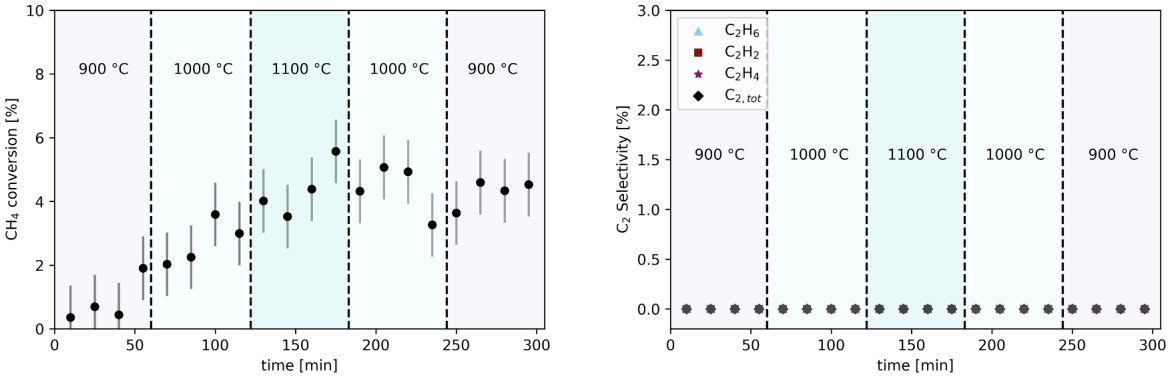


**Figure S9:** Blank Test

Conditions: 10% $CH_4$ in Argon. Total flow 40 mL/min. No formation of $C_2$ species was observed. Margin of error for conversion around 1%.

# 6 Procedure of $^{13}CH_4$ labelling experiment with non-labelled $W^{12}C$ or $Mo_2{}^{12}C$

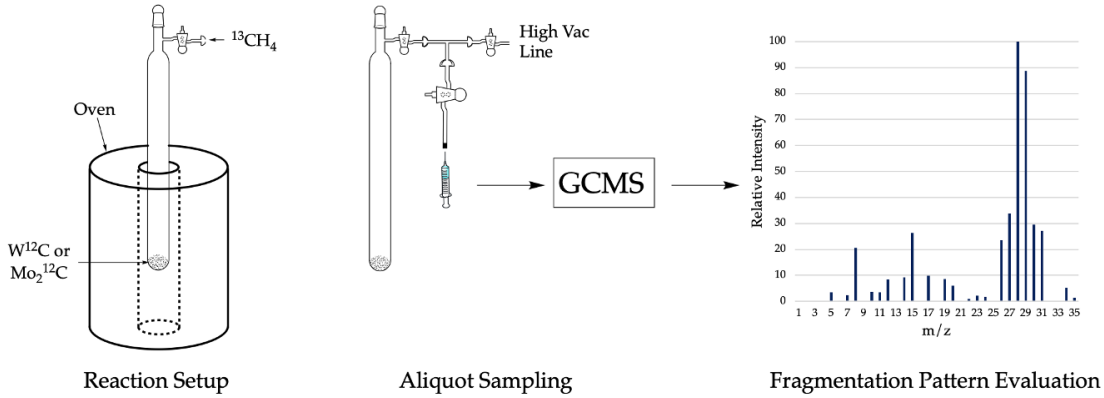


**Figure S10:** Scheme of test setup for experiments with $^{13}CH_4$.

$^{13}CH_4$ labelling experiments were performed for $Mo_2C$ and WC in a batch reactor. 0.5 g of the respective carbide was loaded into a 44 mL quartz glass batch reactor. The reactor was filled with 200 mbar of $^{13}CH_4$ (corresponding to molar ratios of 7.2/1 for WC/$^{13}$CH4 and 6.9/1 for $Mo_2C$/$^{13}$CH4), heated to 1100°C with a heating ramp of 400°C/h and subsequent aliquots were taken with a gas-tight syringe after 3, 6, 9 and 12 h. This corresponds to molar ratios of 7.1:1 for WC: $^{13}CH_4$ and 6.9:1 for $Mo_2C$:$^{13}CH_4$. An aliquot of the gas mixture is taken and analyzed with GCMS resulting in mass fragmentation patterns for $C_2H_6$, $C_2H_4$ and $C_2H_2$. Following a calibration with ethane, ethylene and acetylene, the aliquots were analysed with GCMS to identify the distribution of non-labelled, monolabelled and dilabelled $C_2$ products of the experimental fragmentation patterns. This analysis allowed us to monitor the incorporation of $^{12}C$ into the products which originates to different extents from the carbide and gas phase $^{13}CH_4$.

# 7 Metadynamics Simulations

Ab initio molecular dynamics (AIMD) and metadynamics (MTD) simulations were carried out using the CP2K 5.1 software.[16,17] Molybdenum ($Mo_2C$) and tungsten (WC) bulk was modelled using surface slabs constructed using the reported crystalline orthorhombic (Pbcn)[18] and hexagonal (P6m2)[19] structures respectively. Along the vertical axis the 6-layers slabs were separated by a 10 Å layer of vacuum to avoid self-interactions. The bottom layers of atoms were fixed. The size of the cell ( 10 x 10 x 20 $Å^3$) was considered large enough to account for the electronic structure of the system. Each MTD run was preceded by an unbiased AIMD of 2 ps at 1373 K to ensure thermal equilibration. A MD step length of 1 fs was used. The systems evolved in the NVT canonical ensemble equilibrated using a canonical sampling through velocity rescaling (CSVR) thermostat set at 1373 K with a global temperature tolerance of 20 K. The force field was computed using the revised version of the Perdew-Burke-Ernzerhof PBE functional[20,21] and Grimme dispersion correction D3 with Becket-Johnson (BJ) damping function.[22,23] Atoms were described using single-$\zeta$ molecularly optimized (MOLOPT) gaussian basis sets[24,25] and associated Goedecker-Teter-Hutter GHT pseudopotential.[26] Molecular orbitals occupation numbers were smeared using the Fermi-Dirac method. The free energy surface (FES) related to carbon diffusion in the metal carbide phase was explored by means of metadynamics,[27–31] using a history dependent potential applied along selected collective variables (CVs). In addition to the position on the z axis relatively to a plane described by three atoms belonging to the fixed layers, the coordination numbers from C to C and from C to metal (M = Mo or W) were considered:

$$N^{coord}(C-X) = \sum_i \frac{(1-\frac{r_i}{R_0})^{nn}}{1-\frac{r_i}{R_0})^{nd}} \tag{6}$$

where nn = 12, nd = 24, and $R_0$ corresponds to the C-X bond distance, and takes 1.6 Å for the C-C bonds and 2.3 Å for the C-M ones.

The gaussian bias takes the following form:

$$V(t, s(t)) = w \sum_n e^{-\frac{1}{2}(\frac{s(t)-s(nt_G)}{\delta_S})^2} \tag{7}$$

with $w$ = 1 kcal mol$^1$ ($Mo_2C$) and 2 kcal mol$^1$ (WC) and $\delta_S$ = 0.3, respectively, being the height and width of the Gaussian and $t_G$ = 10 fs being the time interval between two consecutive depositions. The diffusion coefficient at 1373 K were estimated using the following formula:[32]

$$D(T) = \frac{k_B T}{h} l^2 exp(-\frac{\Delta F_d(T)}{k_B T}) \tag{8}$$

With l the distance traveled by the atom, $\Delta F_d$ the free energy of activation, $k_B$ the Boltzmann constant, $h$ the Planck constant and $T$ the temperature.

The free energy of diffusion toward the (001), (010) (see main text) and (011) facets were estimated to test the variability of the simulations. In all cases, the diffusion coefficients obtained in $Mo_2C$ are orders of magnitude higher than those obtained in WC.

Movies of the simulations are available in the ESI (Movies-MTD.zip). In all movies and snapshots carbon is pictured in grey, while molybdenum and tungsten are pictured in lighter and darker shades of blue, respectively.

Remark: Given the nature of this system, full convergence of the free energy surface (FES) cannot be achieved in a reasonable time using molecular dynamics at the DFT level. In order to still obtain qualitatively comparable energy barriers for the different systems, each simulation was ended when the carbon atom reaches a new stable site. No re-crossing of the barrier in the opposite direction was thus considered. This way, the relative heights of the free-energy barrier associated to diffusion were estimated.

**Table S3:** Adatom carbon diffusion Helmholtz free energy barrier, barrier length and coefficients toward the (001), (010) and (011) facets of $Mo_2C$ and WC.

| $Mo_2C$ | $\Delta F^{\ddagger}$ [kcal mol$^{-1}$] | $l$ [Å] | $D$ [m$^2$ s$^{-1}$] |
|---|---|---|---|
| (001) | 56.2 | 2.0 | $1.3 \times 10^{-15}$ |
| (010) | 37.0 | 5.9 | $1.3 \times 10^{-11}$ |
| (011) | 55.4 | 5.2 | $1.2 \times 10^{-14}$ |
| WC | $F$ [kcal mol$^{-1}$] | $l$ [Å] | $D$ [m$^2$ s$^{-1}$] |
| (001) | 143.9 | 5.1 | $9.3 \times 10^{-29}$ |
| (010) | 148.8 | 3.6 | $7.5 \times 10^{-30}$ |
| (011) | 177.9 | 7.5 | $7.7 \times 10^{-34}$ |

## 7.1 $Mo_2C$ (001) facet

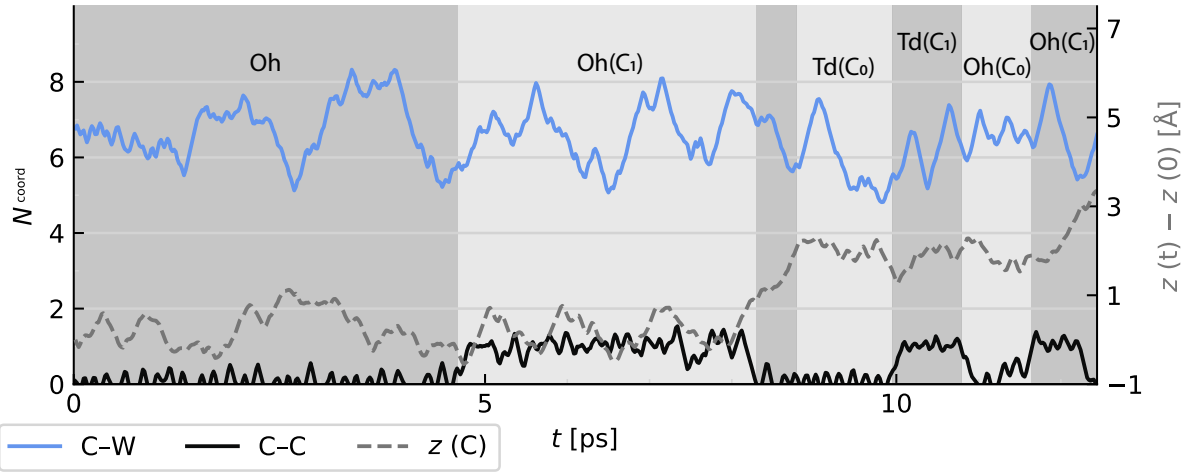


**Figure S11:** Biased coordination numbers and distance along the vertical axis during the metadynamics simulation of $Mo_2C$ where the carbon atom diffuses towards the (001) facet.

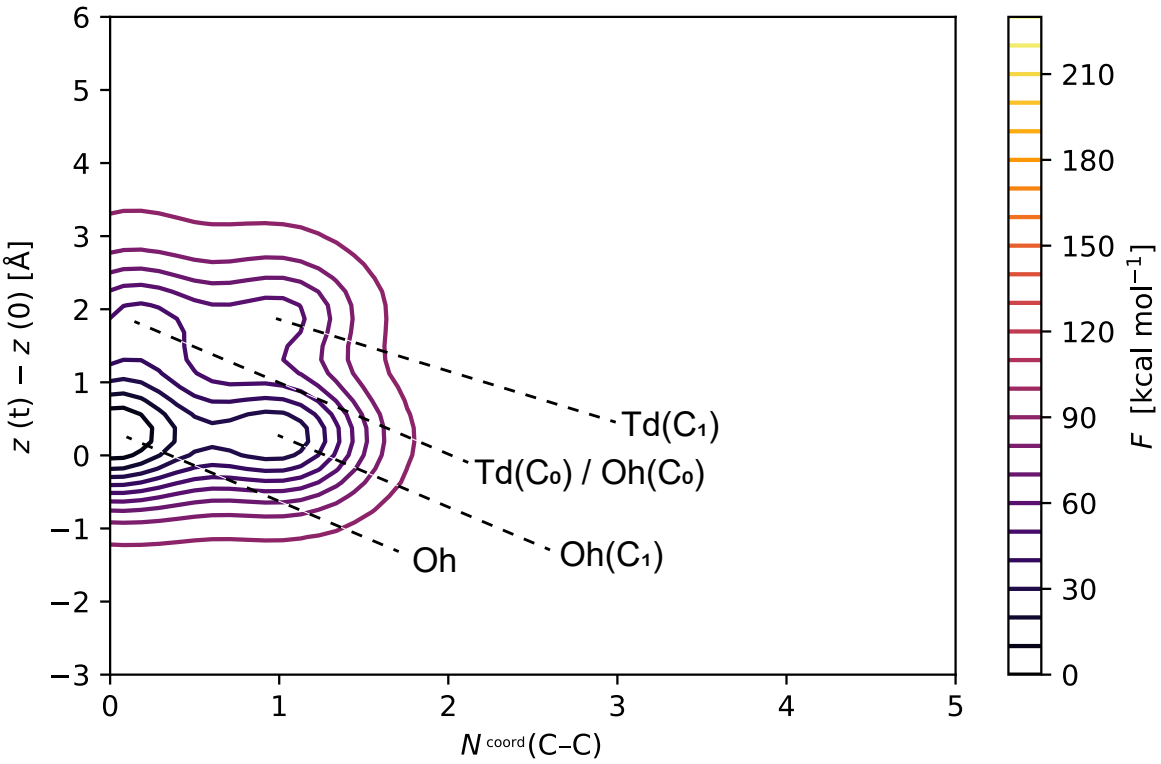


**Figure S 12:** Reconstructed free energy surface projected along the C-C coordination number and z distance from the bottom of the cell for the diffusion of a carbon atom towards the (001) facet of $Mo_2C$.

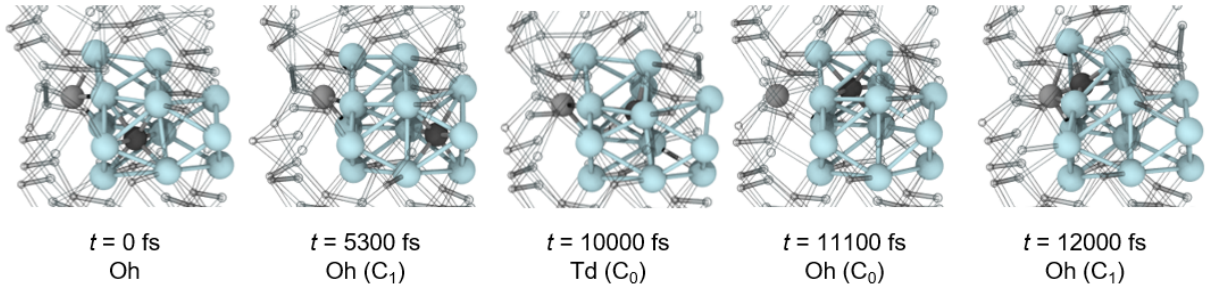


**Figure S13:** Snapshots taken during the simulation highlighting the diffusion of C towards the (001) facet of $Mo_2C$, from the initial octahedral site ($O_h$) via the subsequent vacant octahedral ($O_h$) and tetrahedral sites (Td). The carbon in the $O_h$ ($C_1$) site interacts with another carbon beyond the periodic border.

## 7.2 $Mo_2C$ (011) facet

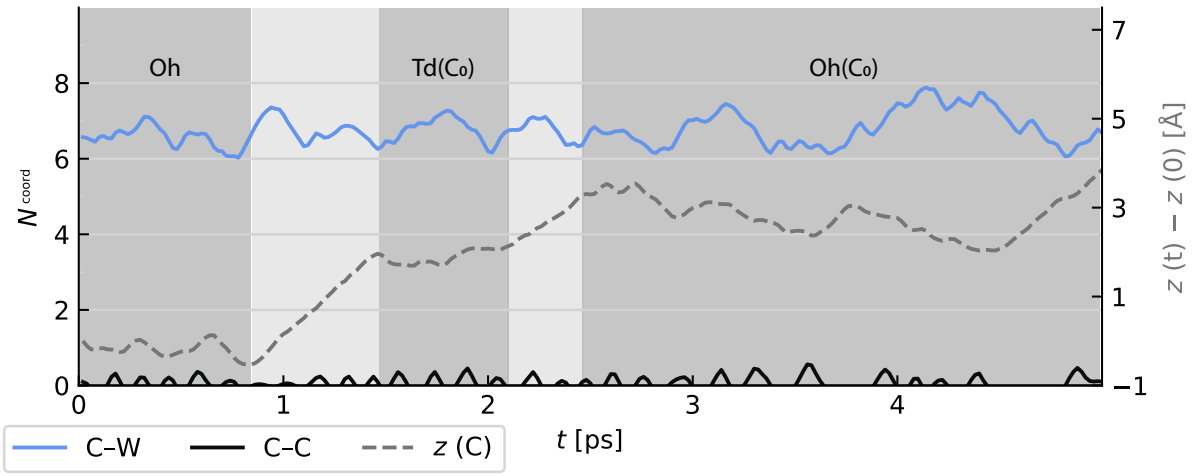


**Figure S14:** Biased coordination numbers and distance along the vertical axis during the metadynamics simulation of $Mo_2C$ where the carbon atom diffuses toward the (011) facet. A fast diffusion is observed for this facet, which is attributed to the lack of C-C interaction during the diffusion process.

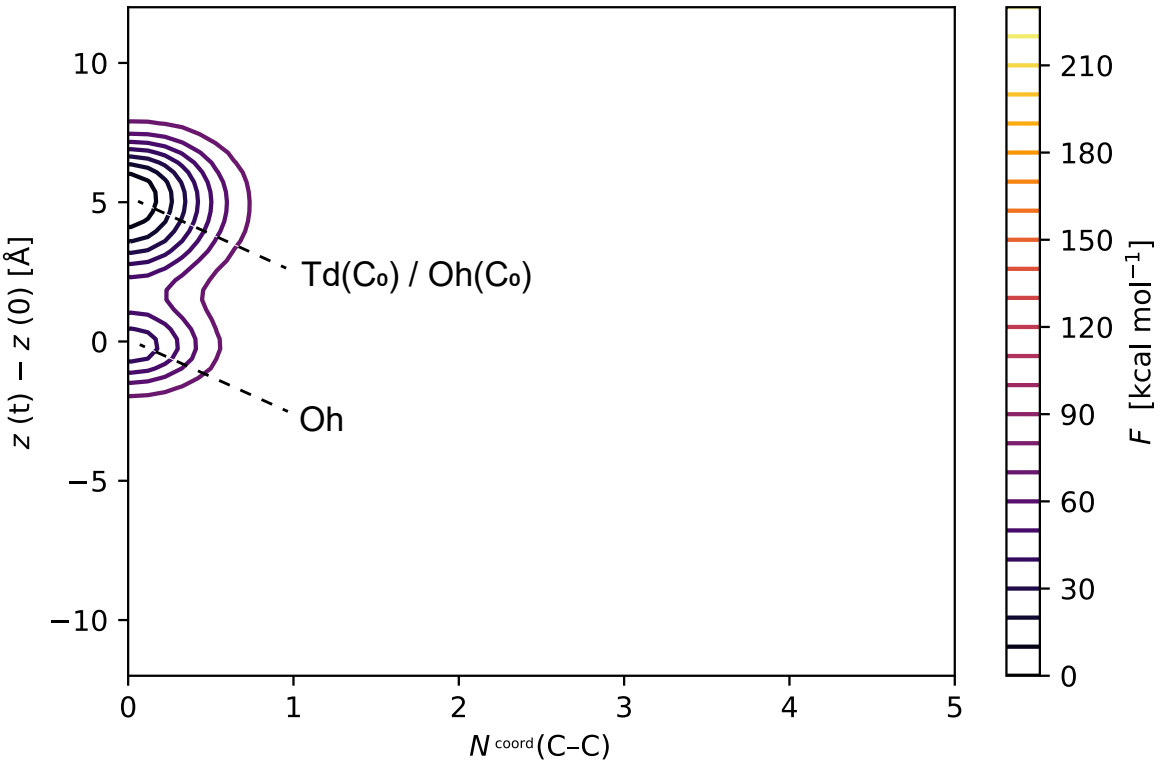


**Figure S 15:** Reconstructed free energy surface projected along the C-C coordination number and z distance from the bottom of the cell for the diffusion of a carbon atom towards the (011) facet of $Mo_2C$. No C-C bonded region is explored before the C atom reaches the surface layer.

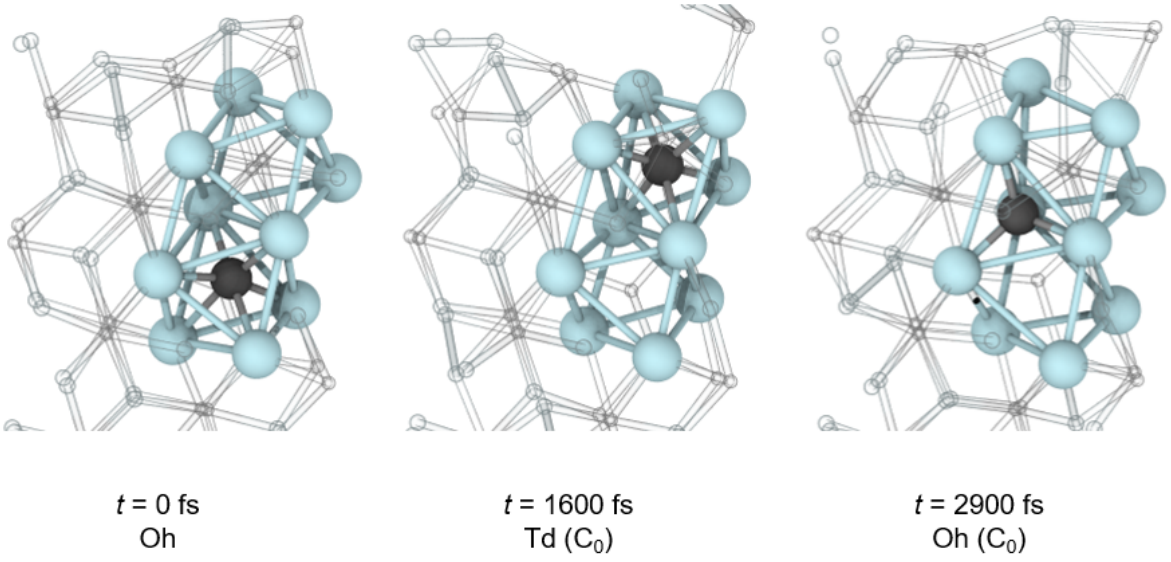


**Figure S16:** Snapshots taken during the simulation highlighting the diffusion of C toward the (011) facet of $Mo_2C$, from the initial octahedral site (Oh) via the subsequent vacant octahedral (Oh) and tetrahedral sites Td.

### 7.3 WC (001) facet

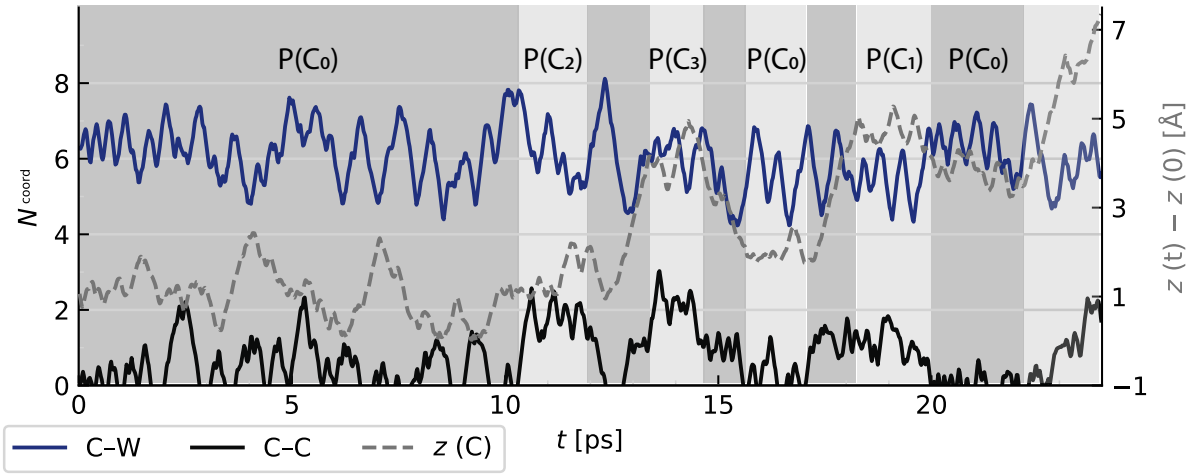


**Figure S17:** Biased coordination numbers and distance along the vertical axis during the metadynamics simulation of WC where a C atom diffuses towards the (001) facet. Diffusion towards the surface takes place via a prismatic (P) ($C_3$ site). At 19 ps, the diffusing C replaces a C occupying a P ($C_0$) site. The displaced carbon diffuses to fill the vacancy, yielding a structure identical to the starting point after 20 ps.

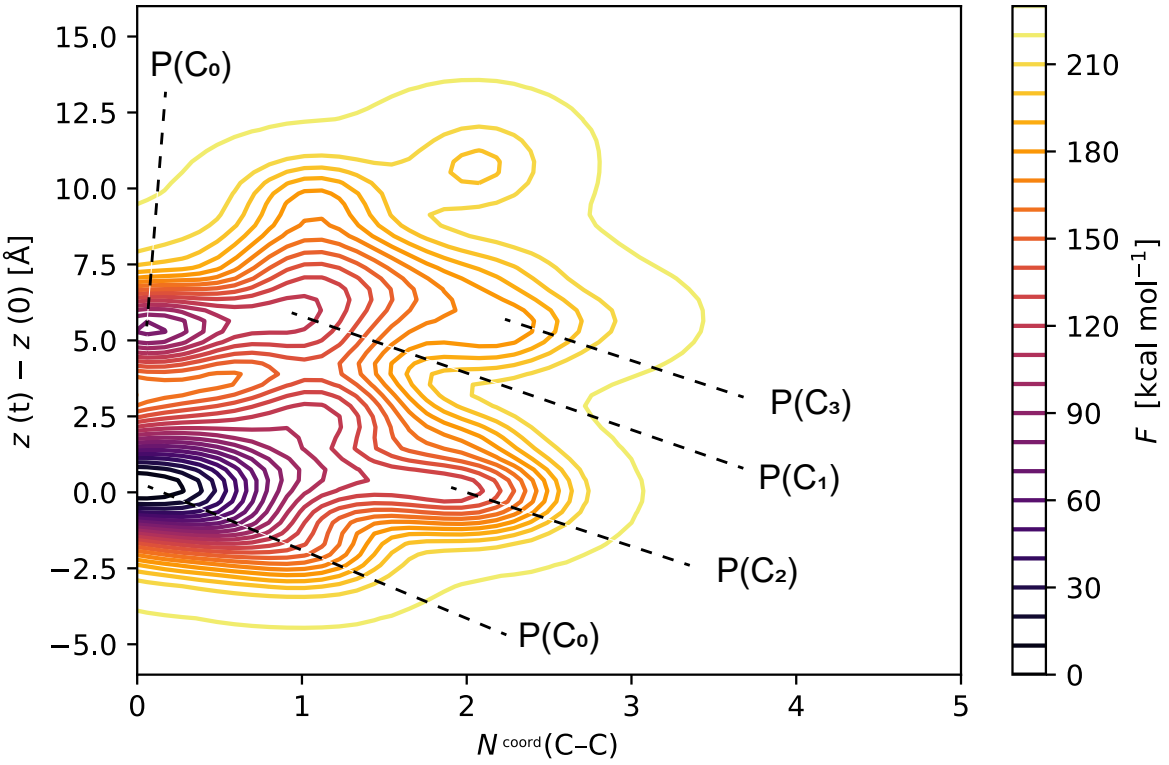


**Figure S 18:** Reconstructed free energy surface projected along the C-C coordination number and z distance from the bottom of the cell for the diffusion of a carbon atom toward the (001) facet of WC. The deep well around 5 Å is attributed to the exchange between the diffusing carbon and the carbon occupying P ($C_0$) site above.

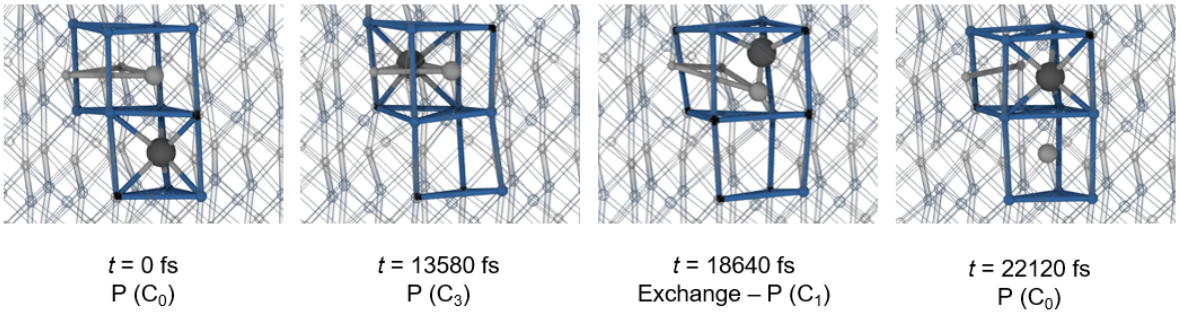


**Figure S19:** Snapshots taken during the simulation highlighting the diffusion of C toward the (001) facet of WC from the initial prismatic site P with no adjacent C (P ($C_0$)), via the subsequent vacant prismatic sites with 2 neighboring C (P ($C_3$)). At 19 ps, the diffusing C replaces a C occupying a P ($C_0$) site. The displaced carbon diffuses to fill the vacancy, yielding a structure identical to the starting point after 20 ps.

## 7.4 WC (011) facet

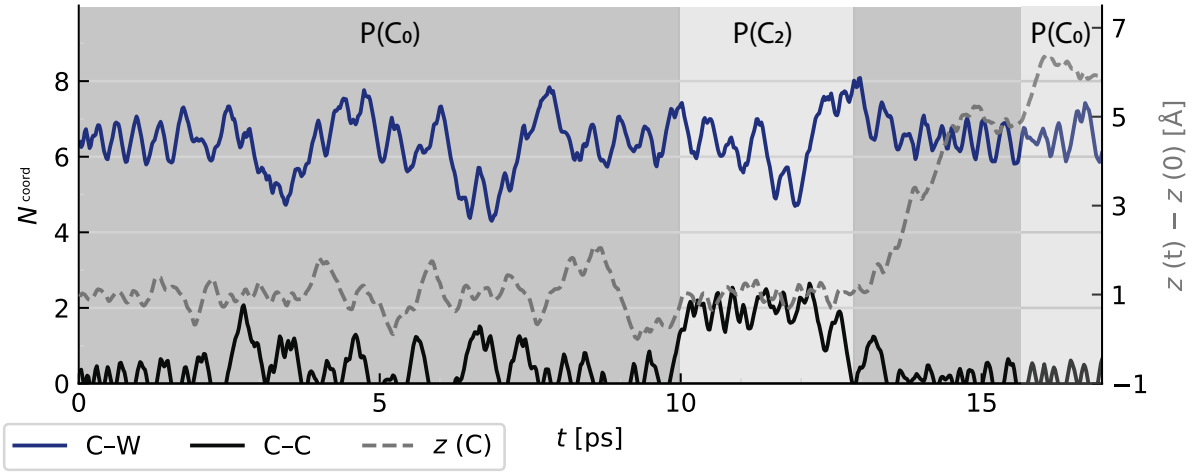


**Figure S20:** Biased coordination numbers and distance along the vertical axis during the metadynamics simulation of WC where the carbon atom diffuses towards the (011) facet.

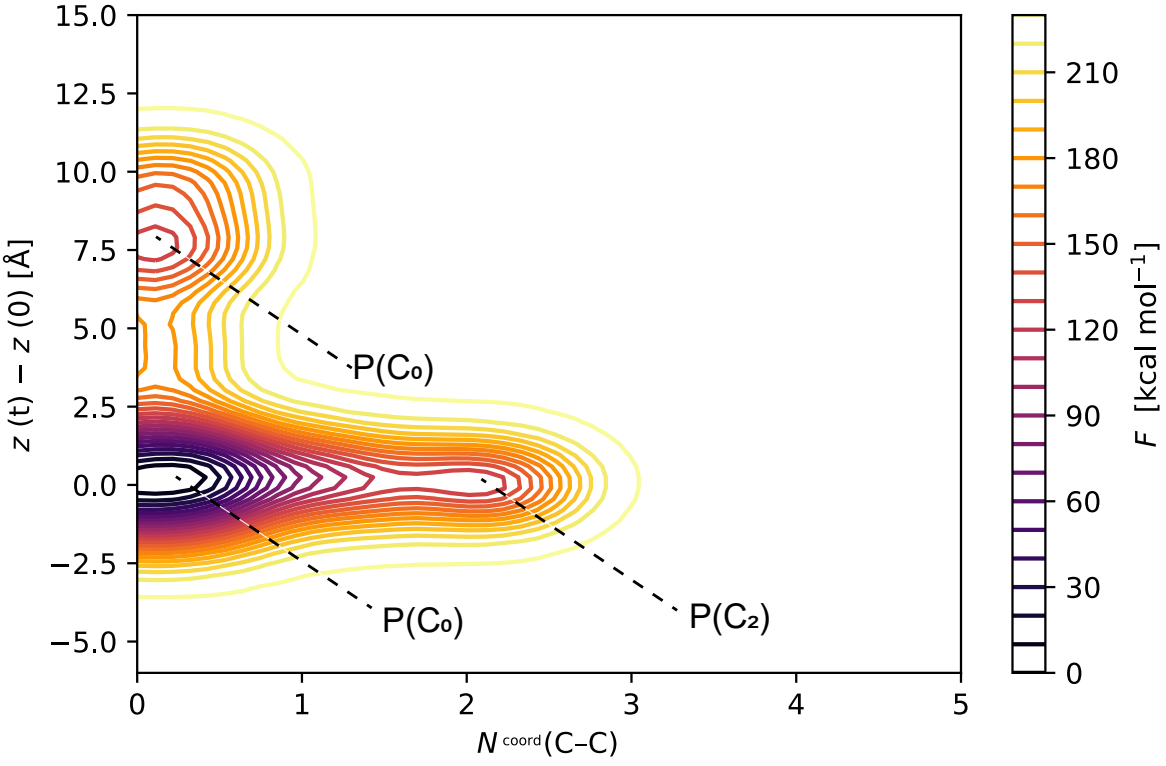


**Figure S 21:** Reconstructed free energy surface projected along the C-C coordination number and z distance from the bottom of the cell for the diffusion of a carbon atom towards the (011) facet of WC.

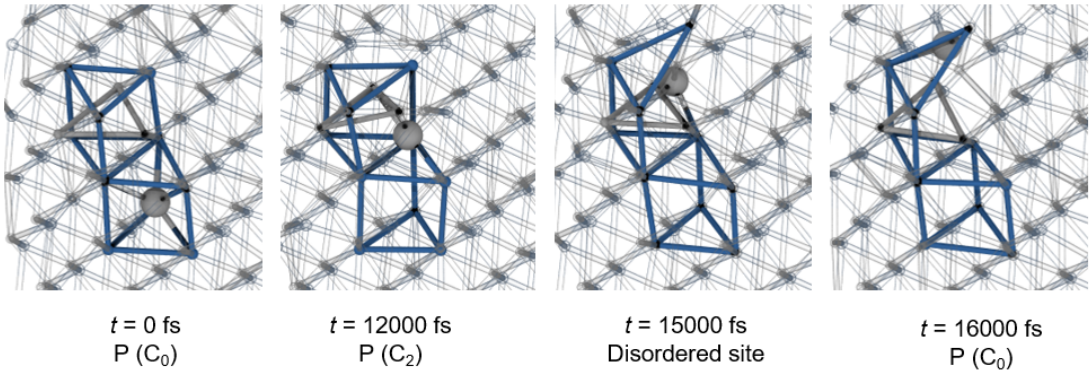


**Figure S 22:** Snapshots taken during the simulation highlighting the diffusion of C towards the (011) facet of WC, from the initial prismatic site p with no adjacent C (P ($C_0$)), then via a disordered site close to the surface.

# 8 Reactivitiy of $Mo_2C$ and WC with $H_2$

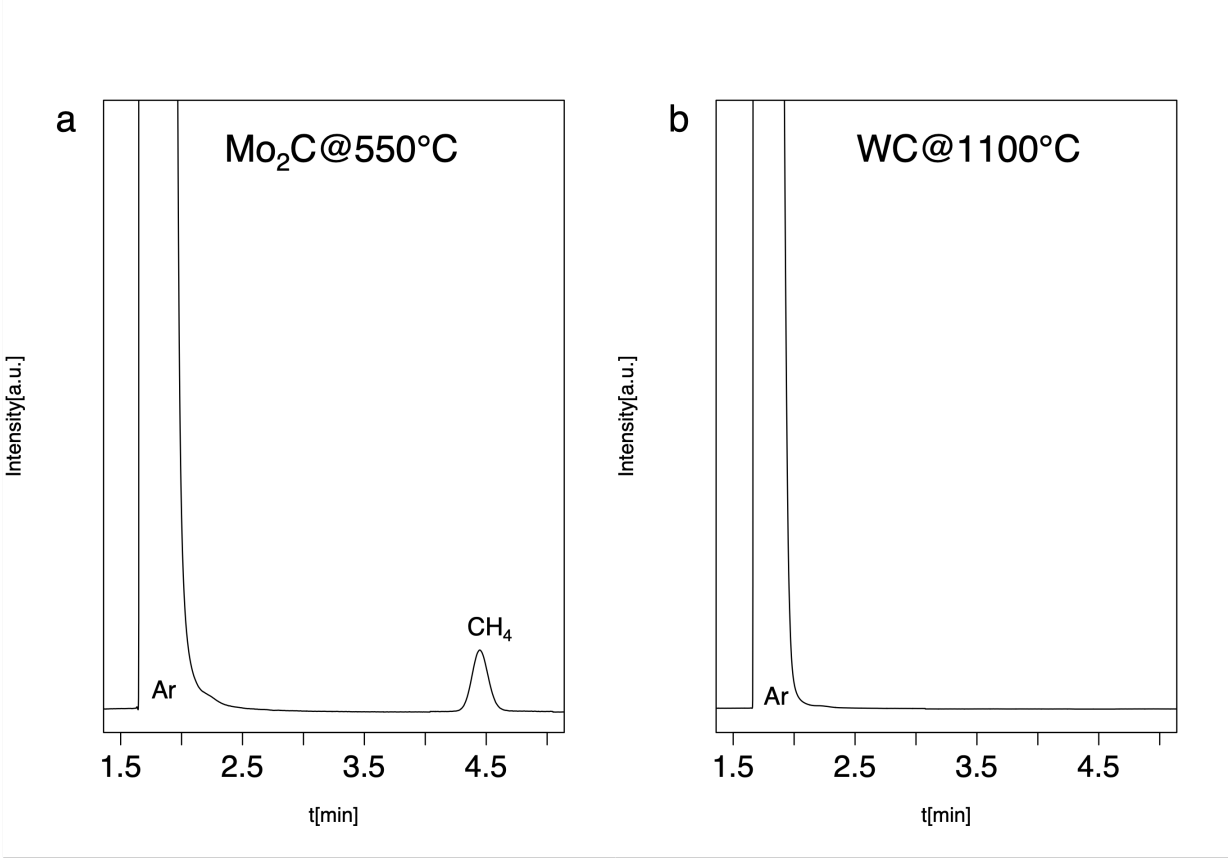


**Figure S23:** GC traces of $Mo_2C$ and WC with $H_2$.

As can be seen in the GC traces for reaction of $H_2$ with $Mo_2C$ the mobility of C and release in the form of $CH_4$ is already shown at 550 °C while WC does not release any $CH_4$ even at 1100 °C.

# References


[1] Wang, L.; Tao, L.; Xie, M.; Xu, G.; Huang, J.; Xu, Y. Dehydrogenation and aromatization of methane under non-oxidizing conditions. *Catalysis Letters* **1993**, *21*, 35–41.

[2] Su, L.; Liu, L.; Zhuang, J.; Wang, H.; Li, Y.; Shen, W.; Xu, Y.; Bao, X. Creating mesopores in ZSM-5 zeolite by alkali treatment: a new way to enhance the catalytic performance of methane dehydroaromatization on Mo/HZSM-5 catalysts. *Catalysis letters* **2003**, *91*, 155–167.

[3] Soulivong, D.; Norsic, S.; Taoufik, M.; Coperet, C.; Thivolle-Cazat, J.; Chakka, S.; Basset, J.-M. Non-Oxidative Coupling Reaction of Methane to Ethane and Hydrogen Catalyzed by the Silica-Supported Tantalum Hydride:( SiO) 2Ta- H. *Journal of the American Chemical Society* **2008**, *130*, 5044–5045.

[4] Szeto, K. C.; Norsic, S.; Hardou, L.; Le Roux, E.; Chakka, S.; Thivolle-Cazat, J.; Baudouin, A.; Papaioannou, C.; Basset, J.-M.; Taoufik, M. Non-oxidative coupling of methane catalysed by supported tungsten hydride onto alumina and silica–alumina in classical and H 2 permeable membrane fixed-bed reactors. *Chemical Communications* **2010**, *46*, 3985–3987.

[5] Guo, X. *et al.* Direct, nonoxidative conversion of methane to ethylene, aromatics, and hydrogen. *Science (New York, N.Y.)* **2014**, *344*, 616–9.

[6] Sakbodin, M.; Wu, Y.; Oh, S. C.; Wachsman, E. D.; Liu, D. Hydrogen-Permeable Tubular Membrane Reactor: Promoting Conversion and Product Selectivity for Non-Oxidative Activation of Methane over an Fe©SiO2Catalyst. *Angewandte Chemie - International Edition* **2016**, *55*, 16149–16152.

[7] Xie, P.; Pu, T.; Nie, A.; Hwang, S.; Purdy, S. C.; Yu, W.; Su, D.; Miller, J. T.; Wang, C. Nanoceria-Supported Single-Atom Platinum Catalysts for Direct Methane Conversion. *ACS Catalysis* **2018**, *8*, 4044–4048.

[8] Xiao, Y.; Varma, A. Highly Selective Nonoxidative Coupling of Methane over Pt-Bi Bimetallic Catalysts. *ACS Catalysis* **2018**, *8*, 2735–2740.

[9] Oh, S. C.; Schulman, E.; Zhang, J.; Fan, J.; Pan, Y.; Meng, J.; Liu, D. Direct non-oxidative methane conversion in a millisecond catalytic wall reactor. *Angewandte Chemie* **2019**, *131*, 7157–7160.

[10] Šot, P.; Newton, M. A.; Baabe, D.; Walter, M. D.; van Bavel, A. P.; Horton, A. D.; Copéret, C.; van Bokhoven, J. A. Non-oxidative methane coupling over silica versus silica-supported iron (II) single sites. *Chemistry–A European Journal* **2020**,

[11] Deng, M.; Qi, J.; Li, X.; Xiao, Y.; Yang, L.; Yu, X.; Wang, H.; Yuan, B.; Gao, Q. MoC/C nanowires as high-rate and long cyclic life anode for lithium ion batteries. *Electrochimica Acta* **2018**, *277*, 205–210.

[12] Oshikawa, K.; Nagai, M.; Omi, S. Characterization of molybdenum carbides for methane reforming by TPR, XRD, and XPS. *The Journal of Physical Chemistry B* **2001**, *105*, 9124–9131.

[13] Wang, D.; Lunsford, J. H.; Rosynek, M. P. Characterization of a Mo/ZSM-5 catalyst for the conversion of methane to benzene. *Journal of Catalysis* **1997**, *169*, 347–358.

[14] Solymosi, F.; Cserényi, J.; Szöke, A.; Bánsági, T.; Oszkó, A. Aromatization of methane over supported and unsupported Mo-based catalysts. *Journal of Catalysis* **1997**, *165*, 150–161.

[15] Ohnishi, R.; Liu, S.; Dong, Q.; Wang, L.; Ichikawa, M. Catalytic dehydrocondensation of methane with CO and CO2toward benzene and naphthalene on Mo/HZSM-5 and Fe/Co-modified Mo/HZSM-5. *Journal of Catalysis* **1999**, *182*, 92–103.

[16] Kühne, C. An electronic structure and molecular dynamics software package-Quickstep: Efficient and accurate electronic structure calculations. *J. Chem. Phys*

[17] Hutter, J.; Iannuzzi, M.; Schiffmann, F.; VandeVondele, J. cp2k: atomistic simulations of condensed matter systems. *Wiley Interdisciplinary Reviews: Computational Molecular Science* **2014**, *4*, 15–25.

[18] Parthé, E.; Sadogopan, V. The structure of dimolybdenum carbide by neutron diffraction technique. *Acta Crystallographica* **1963**, *16*, 202–205.

[19] Page, K.; Li, J.; Savinelli, R.; Szumila, H. N.; Zhang, J.; Stalick, J. K.; Proffen, T.; Scott, S. L.; Seshadri, R. Reciprocal-space and real-space neutron investigation of nanostructured Mo2C and WC. *Solid State Sciences* **2008**, *10*, 1499–1510.

[20] Perdew, J. P.; Burke, K.; Ernzerhof, M. Generalized gradient approximation made simple. *Physical review letters* **1996**, *77*, 3865.

[21] Zhang, Y.; Yang, W. Comment on "Generalized gradient approximation made simple". *Physical Review Letters* **1998**, *80*, 890.

[22] Grimme, S.; Antony, J.; Ehrlich, S.; Krieg, H. A consistent and accurate ab initio parametrization of density functional dispersion correction (DFT-D) for the 94 elements H-Pu. *The Journal of chemical physics* **2010**, *132*, 154104.

[23] Grimme, S.; Ehrlich, S.; Goerigk, L. Effect of the damping function in dispersion corrected density functional theory. *Journal of computational chemistry* **2011**, *32*, 1456–1465.

[24] Lippert, B. G.; PARRINELLO, J. H.; MICHELE, A hybrid Gaussian and plane wave density functional scheme. *Molecular Physics* **1997**, *92*, 477–488.

[25] VandeVondele, J.; Hutter, J. Gaussian basis sets for accurate calculations on molecular systems in gas and condensed phases. *The Journal of chemical physics* **2007**, *127*, 114105.

[26] Krack, M. Pseudopotentials for H to Kr optimized for gradient-corrected exchange-correlation functionals. *Theoretical Chemistry Accounts* **2005**, *114*, 145–152.

[27] Laio, A.; Parrinello, M. Escaping free-energy minima. *Proceedings of the National Academy of Sciences* **2002**, *99*, 12562–12566.

[28] Barducci, A.; Bonomi, M.; Parrinello, M. Metadynamics. *Wiley Interdisciplinary Reviews: Computational Molecular Science* **2011**, *1*, 826–843.

[29] Barducci, A.; Bussi, G.; Parrinello, M. Well-tempered metadynamics: a smoothly converging and tunable free-energy method. *Physical review letters* **2008**, *100*, 020603.

[30] Valsson, O.; Tiwary, P.; Parrinello, M. Enhancing important fluctuations: Rare events and metadynamics from a conceptual viewpoint. *Annu. Rev. Phys. Chem* **2016**, *67*, 159–184.

[31] others„ *et al.* Free-energy calculations with metadynamics: Theory and practice. *Rev. Comput. Chem* **2015**, *28*, 1–49.

[32] Kürpick, U.; Kara, A.; Rahman, T. S. Role of lattice vibrations in adatom diffusion. *Physical review letters* **1997**, *78*, 1086.